Canted antiferromagnetism in high-purity NaFeF$_3$ prepared by a novel wet-chemical synthesis method

Fabian L. M. Bernal, Bruno Gonano, Fredrik Lundvall, David S. Wragg, and Helmer Fjellvåg[*]
Chemistry Department and Center for Material Science and Nanotechnology, University of Oslo, NO-0315 Oslo, Norway

Fabien Veillon
Laboratory Crismat, UMR6508 CNRS, Normandie University, ENSICAEN, UNICAEN, 6 bd Maréchal Juin, 1450 Caen cedex 4, France

Wojciech A. Sławiński
Faculty of Chemistry, University of Warsaw, Pasteura 1, 02-093 Warsaw, Poland
and ISIS Facility, Rutherford Appleton Laboratory, Harwell Oxford, Didcot, Oxfordshire OX11 0QX, United Kingdom

Øystein S. Fjellvåg
Department for Neutron Materials Characterization, Institute for Energy Technology, PO Box 40, NO-2027 Kjeller, Norway

We report a synthesis method, and structural and magnetic characterization, for the fluoroperovskite NaFeF$_3$. We have developed a wet-chemical method that allows preparation of large volumes of air-sensitive fluoroperovskites with high purity. NaFeF$_3$ has a Néel temperature (T_N) of 90 K and a Weiss constant (θ) of -124 K, corresponding to dominant antiferromagnetic interactions. Below T_N, a slight difference is observed between zero-field and field-cooled samples, indicating spin canting and weak ferromagnetism. AC magnetometry supports that weak ferromagnetism is inherent to NaFeF$_3$ and not due to an impurity. From powder neutron diffraction data, we describe the magnetic structure precisely as a weakly canted G-type (magnetic space group $Pn'ma'$). A ferromagnetic component is allowed in $Pn'ma'$, however, this component is too small to be confirmed on the basis of powder neutron diffraction data and may be absent in zero magnetic fields.

I. INTRODUCTION

Fluoroperovskites display rich structural chemistry, strongly ionic bonding character (due to the high electronegativity of the fluoride anions), and corresponding localized electron magnetism [1,2]. They exhibit a wide range of properties that can be utilized in, e.g., data storage, computer processors, spintronics, multiferroics, and batteries [3–6].

NaFeF$_3$ has attracted attention as a low-cost cathode material [7,8]. Its advantages in this application include the Earth's abundance of the constituent elements, intrinsic anion stability, and a theoretical capacity of 197 m A hg^{-1} for a one-electron process. NaFeF$_3$ nanoplates in particular show good capacity retention compared to other metal fluoride and composite cathode materials, with 50% retained capacity for Na after 200 cycles at 0.2 A g^{-1} [9].

The NaFeF$_3$ fluoroperovskite has intriguing phase relations under high pressure. At ambient temperature and pressure, the compound adopts the orthorhombic perovskite GdFeO$_3$-type crystal structure with space group $Pnma$. It transforms into a corrugated layered CaIrO$_3$-type post-perovskite (pPv) structure at room temperature at 9 GPa [10]. A second structural phase transition occurs at 20 GPa from pPv to ppPv with the Sb$_2$S$_3$-type crystal structure [11]. The remarkable structural flexibility of NaFeF$_3$ has made it an interesting candidate for studies and simulations of extreme environments, including the Earth's interior and exoplanets [12].

The electronic configuration of the Fe^{2+} ions in NaFeF$_3$ is high-spin (HS) $t_{2g}^4 e_g^2$. They follow the spin-only model with $S = 2$ and a theoretical paramagnetic moment of $\mu_{eff} = 4.90 \, \mu_B$, which is influenced by orbital contributions and usually leads to slightly higher μ_{eff}.

Fe^{2+} is air sensitive and oxidizes easily to Fe^{3+}. Controlling the anaerobic chemistry of Fe^{2+} ions is a prerequisite for synthesis of single-phase NaFeF$_3$. We have previously utilized a solid-state synthesis under inert conditions [10], yielding a sample with <0.5 % Fe metal impurity. Impurities, either from an incomplete solid-state reaction of the reagents or from the iron reaction vessel, may introduce inaccuracy to magnetometric studies and disguise the inherent magnetic behavior of NaFeF$_3$. Indeed, to the best of our knowledge there are no neutron powder diffraction (NPD) studies on the magnetic ordering in NaFeF$_3$, probably because the air sensitivity of Fe^{2+} makes it very difficult to produce sample volumes sufficient for NPD experiments by conventional solid-state methods.

In this article we describe a wet-chemistry synthesis method for NaFeF$_3$, which produces iron-free material in substantial volumes. Using the high-purity NaFeF$_3$ samples,

---

[*]helmer.fjellvag@kjemi.uio.no

we study the intrinsic magnetic properties of the compound. Further, the magnetic structure is precisely described based on neutron powder diffraction data.

II. EXPERIMENTAL

A. Synthesis of NaFeF$_3$

NaFeF$_3$ was synthesised on a Schlenk line equipped with flexible hoses. Two polycarbonate vials of 85 and 200 ml volume (denoted A and B, respectively) were used for the reaction. Vial A was filled with 2 g of Fe powder ($\sim$0.035 g mol^{-1}, 99.999% pure) and vial B with 0.08 mol ($\sim$3.35 g) NaF. The vials were closed tightly with silicone rubber septa, connected through the hoses to the Schlenk line, and thoroughly flushed with Ar. The Ar flow was maintained throughout the reaction to ensure inert conditions. A needle was placed in each septum to vent the excess gas from the vials. 10 mL of HCl (37%) and 20 mL H$_2$O were degassed, mixed, and added to vial A. 20 mL of degassed H$_2$O was carefully injected (using a syringe first evacuated and flushed with Ar) to the NaF in vial B. Both vials were placed in an oil bath under constant Ar flow at 90°C until the oxidation of Fe metal to FeCl$_2$ was completed. The FeCl$_2$ solution from vial A was then quickly transferred to vial B with an Ar flushed syringe. The contents of vial B were stirred constantly during injection to mix the two solutions. Thereafter, vial B was cooled to 80°C and the contents stirred for 30 to 60 minutes. NaFeF$_3$ appeared as a beige precipitate. The product was washed repeatedly with degassed water and MeOH under flowing Ar, with decanting of the liquid after each washing. Finally, the solid product was removed from the vial, filtered, washed thoroughly with degassed MeOH, and dried under vacuum overnight before storing in the Ar atmosphere of a glove box. Phase purity was confirmed by powder x-ray diffraction (PXRD) and magnetometry.

B. Powder x-ray diffraction

PXRD data for NaFeF$_3$ was collected at the Norwegian National Resource Centre for X-ray Diffraction, Scattering and Imaging (RECX) on a Bruker D8 A25 powder diffractometer in capillary mode using Mo radiation and a focusing mirror. A Lynxeye detector with "hardened" chip for Mo radiation was used for the data collection. The diffraction patterns were analyzed using TOPAS V5 [13], where the background (16-term Chebyshev polynomials), zero error, lattice parameters, atomic positions, peakshape, common isotropic thermal displacement parameters for all elements, and scale factor were refined.

C. Magnetic characterization

Magnetometry experiments were performed with a 9 T Physical Property Measurement System (PPMS, Quantum Design) on 48 mg of polycrystalline powder. Temperature-dependent DC magnetic susceptibility $\chi(T)$ measurements were conducted between 2 and 300 K for zero-field cooled samples, followed by studies at field cooled conditions (ZFC and FC, respectively). The magnetic susceptibility is calculated by $\chi = M/H$, where M is the magnetization given

in emu mol^{-1}Oe^{-1} and H the magnetic field (10 kOe). Isothermal field-dependent measurements $M(H)$ were collected at 2K, likewise half-loop isothermal measurements at 70, 120, and 300 K, all up to 90 kOe. AC measurements were carried out with frequencies ranging from 100 Hz to 10 kHz with a 10 Oe field.

D. Neutron Powder Diffraction

NPD data for NaFeF$_3$ was measured on the WISH instrument at the ISIS pulsed neutron and muon source (UK) [14]. Diffraction patterns were collected between 2 and 297 K, and the data was reduced with the MANTID software [15]. Data from the four highest resolution detector banks were used, as the lowest resolution bank did not contain any unique information. NPD was collected at selected temperatures below and above T_N.

The magnetic refinements were carried out in the magnetic space group $Pn'ma'$, which allows non-zero values for M_x, M_y, and M_z, in the JANA2006 software [16]. The background (five-term Legendre polynomials), peak-shape, atomic positions (according to symmetry restrictions), isotropic thermal displacement parameters for each element type, lattice parameters, and scale parameters were refined. The derived values for M_x and M_z are given in the Supplemental Material [17].

III. RESULTS

A. Synthesis procedure and crystal structure

Fluoroperovskites are typically prepared by solid-state reactions and may contain magnetic impurities that make them appear as weak ferromagnets, both below and above the Néel temperature, as α-Fe impurities in NaFeF$_3$ [10]. The air-sensitive chemistry of fluoroperovskites is furthermore demanding. We currently benefit from a new wet-chemical method that bypasses the challenges of conventional solid-state reactions by always working under inert conditions on a Schlenk line. This wet-chemistry approach is ideal for synthesis of air-sensitive fluorides, as recently shown for the extremely air-sensitive Cr^{2+} [18].

The weakly beige fluoroperovskite NaFeF$_3$ is currently prepared by means of this wet-chemical method, and the purity was confirmed by XRD and NPD, see the Supplemental Material [17]. For XRD and NPD, a tiny peak at $d = 4.92$ Å ($Q = 1.28$ Å^{-1}) is observed with unknown origin, and for NPD, a peak from the vanadium can is observed at $d = 2.14$ Å. We can exclude that the peak originates in metallic Fe, Fe$_3$O$_4$, Fe$_2$O$_3$, FeF$_2$, FeF$_3$, NaFeO$_2$, etc. Except for this, no reflections from impurities are observed, and we consider the sample to be of very high purity. Due to the high quality and good contrast of the NPD from the WISH instrument at ISIS pulsed neutron and muon source, we will continue the structural discussion based on these data.

Rietveld refinements of NPD data at 297 K yield lattice parameters of $a = 5.66227(7)$ Å, $b = 7.88227(10)$ Å, and $c = 5.48661(7)$ Å, which are in perfect compliance with reports [9,10], confirming the correct stoichiometry of the sample. Rietveld refinements of the composition revealed no variations outside the standard deviations. The composition is
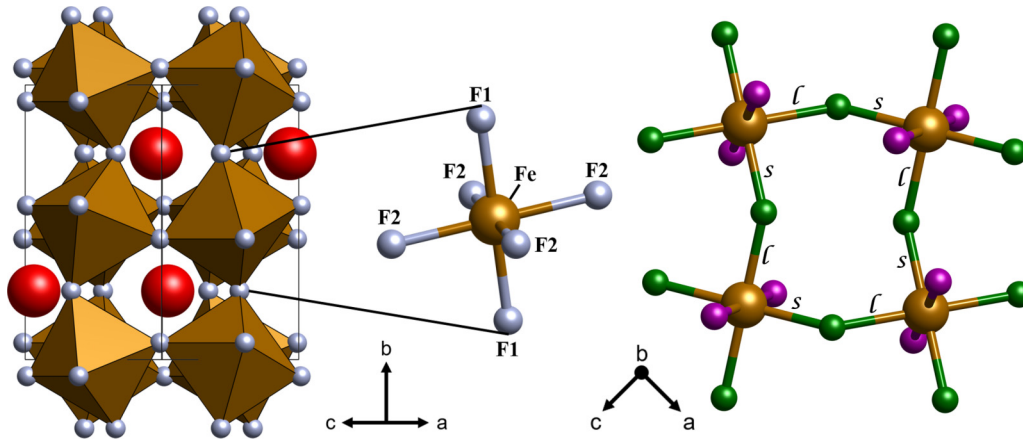
FIG. 1. Crystal structure of the orthorhombic perovskite $NaFeF_3$ (*Pnma*). Left: Illustration of the corner-connected octahedra of FeF_6 with Glazer tilt $a^-b^+a^-$. Sodium, iron, and fluorine atoms are shown in red, orange, and gray, respectively. Right: Illustration of the *ac*-plane, where ordered short and long Fe-F2 bonds are formed by the weak Jahn-Teller effect. The short and long Fe-F2 bonds are marked *s* and *l*, respectively, while medium Fe-F1 bonds are out of plane. Fe, F1, and F2 are shown in orange, purple, and green, respectively.

further in excellent agreement with magnetic measurements, see below.

$NaFeF_3$ adopts the distorted orthorhombic $GdFeO_3$ perovskite structure with space group *Pnma* and Glazer tilt $a^-b^+a^-$, see Fig. 1. The relation to the ideal cubic perovskite is given by $a \approx c \approx \sqrt{2}a_c$ and $b \approx 2a_c$, where a_c is the lattice parameter of the cubic perovskite. A weak Jahn-Teller distortion is present in the system originating from the high-spin d^6 electron configuration of Fe^{2+}. The consequence of the weak Jahn-Teller effect is slight differences in the bond lengths; the Fe-F1 bonds adopt a medium length (2.0744(3) Å), while Fe-F2 forms two short and two long bonds (2.0564(6) Å and 2.0795(6) Å, respectively), see Fig. 1. Bond length values are extracted from NPD at 297 K, see below.

B. Magnetic properties

Variable-temperature DC magnetization measurements were carried out on a polycrystalline sample between 2 and 300 K under a 10 kOe field (see Fig. 2). The data are consistent with long-range antiferromagnetic ordering. A sharp decrease in the molar magnetic susceptibility is associated with a Néel transition at 90 K. From the inverse susceptibility χ^{-1} curve in the paramagnetic region (200 to 300 K), we calculate a paramagnetic moment of $\mu_{eff} = 5.58\mu_B$ from the Curie-Weiss fit shown in Fig. 2. This is in good agreement with typically observed values for Fe^{2+} (5.0 − 5.6 μ_B). From the Curie-Weiss fit, we extract a Weiss-temperature of $\theta = -124$ K (data measured in a field of 10 kOe), confirming the dominating antiferromagnetic nature of $NaFeF_3$.

We note a significant difference between the FC and ZFC curves at low temperatures, as well as a minor hysteresis. This might indicate a transition to a spin-glass-like state at low temperatures. However, AC magnetization measurements [Fig. 3(a)] in a 10 Oe field show no variations of the Néel temperature versus frequency for χ', refuting this hypothesis.

The appearance of magnetic hysteresis may be explained by the presence of a small ferromagnetic moment originating from spin canting, resulting in weak ferromagnetism. For a purely antiferromagnetic transition, the imaginary component

χ'' is expected to be zero in AC measurements [19]. In contrast, for χ'' [Fig. 3(b)] we observe a strong peak for an AC field of 10 kHz, indicating that the magnetic transition at 90 K is not purely antiferromagnetic and that a small ferromagnetic component is present. The peak is less pronounced for the 1 kHz AC field, while only noise is observed for the 100 Hz AC field.

As the peak starts to increase in intensity at the Néel temperature (90 K), we believe that the peak is associated with the magnetic transition in $NaFeF_3$, and we exclude effects caused by an impurity, such as α-Fe, Fe_3O_4 and other ferromagnetic compounds with high (> 90 K) Curie temperature. Consequently, it is evident that spin canting results in weak ferromagnetism in $NaFeF_3$ that is inherent to the compound. We note that the ferromagnetism is very weak and based on DC (Fig. 2) and AC (Fig. 3) magnetometry, it should be very
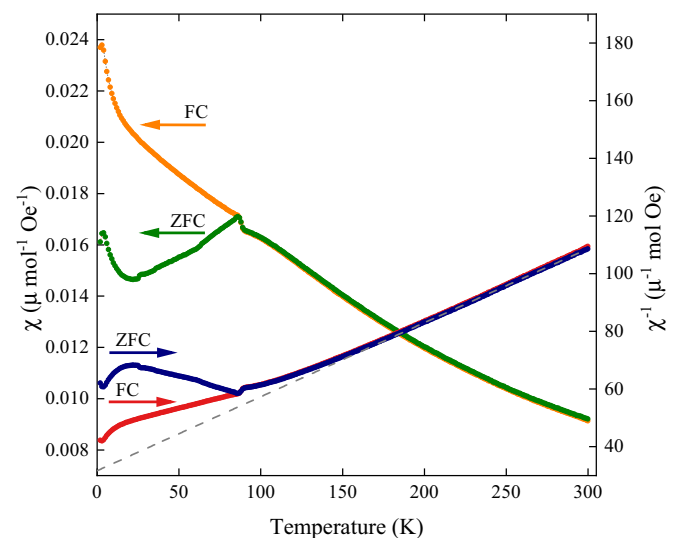

FIG. 2. Temperature dependency of the magnetic susceptibility $\chi(T)$ at $H = 10$ kOe measured in ZFC-FC mode (left axis) and inverse magnetic susceptibility χ^{-1} (right axis). The Curie-Weiss fit is shown as a dashed gray line.
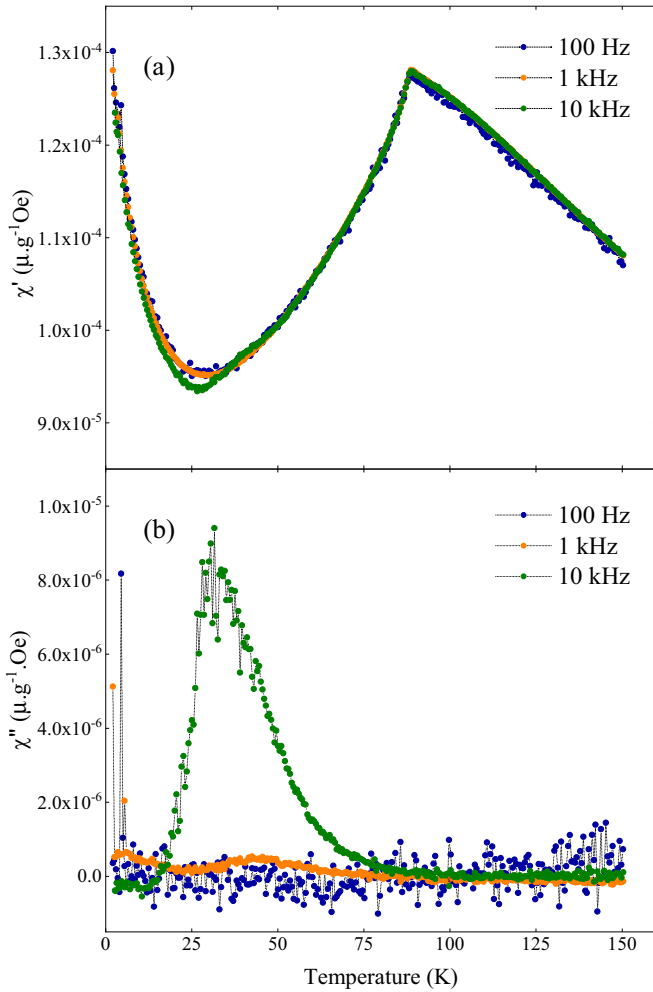
FIG. 3. Temperature dependence of the (a) real (χ') and (b) imaginary (χ'') part of the AC magnetic susceptibility at different frequencies (100 Hz, 1 kHz, and 10 kHz).

FIG. 4. Isothermal M versus H curves with an applied field 0 T → 9 T → 0 T recorded at 2, 70, 120, and 300 K. Insert: M versus H curve at 2 K to show the full symmetry.

2 K, strong additional reflections from long-range magnetic ordering are evident, e.g., two strong reflections at 4.49 and 4.58 Å, and one weaker reflection at 7.89 Å (Fig. 5). To identify reflections of magnetic origin, diffraction patterns measured above and below the Néel temperature are given in the Supplemental Material [17]. These reflections were indexed according to the unit cell of the crystal structure of $NaFeF_3$ and correspond to a Γ-point magnetic propagation vector $k = (0, 0, 0)$. However, several of the observed magnetic reflections break the symmetry extinctions of space group *Pnma*. We hence evaluated the possible magnetic structures for the

close to zero in the absence of a magnetic field. The maximum of the peak is at ∼32 K, indicating that the spin canting is further developing below the Néel temperature until the peak goes to zero at ∼13 K.

Isothermal field-dependent magnetic measurements above the Néel temperature ($T_N = 90$ K) at 120 and 300 K show a linear behavior, associated with a paramagnetic state (Fig. 4). The low magnetization observed at 90 kOe ($0.25 \mu_B$/Fe at 2 K) confirms the dominating antiferromagnetic behavior of the system. However, below the Néel temperature, a slight hysteresis is observed. The hysteresis is more clear at 2 K (inset in Fig. 4), while it is less prominent at 70 K. The presence of hysteresis below T_N supports that weak ferromagnetism is intrinsic to the compound, as indicated by χ'' in AC magnetometry. Enlarged isothermal field-dependent magnetic measurements are given in the Supplemental Material for visualization of the hysteresis [17].

C. Neutron diffraction and magnetic structure

Neutron diffraction was carried out between 2 and 297 K to investigate possible ordering of Fe^{2+} magnetic moments. At
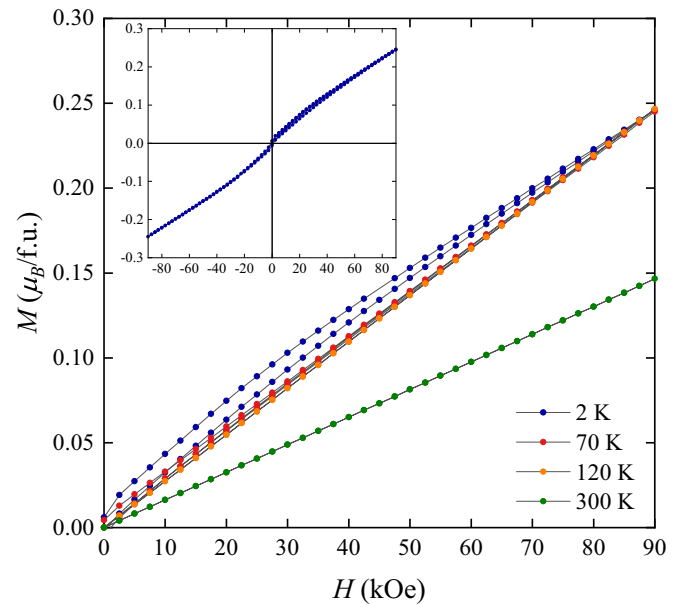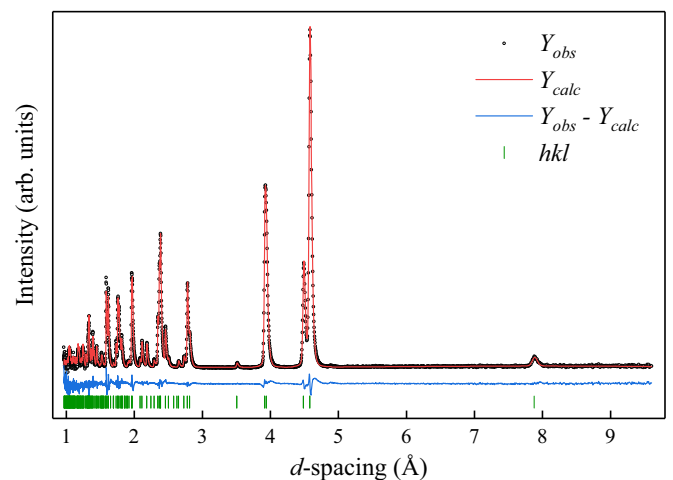

FIG. 5. Measured, calculated, and difference curves from Rietveld refinement of the magnetic structure of $NaFeF_3$ at 2 K for the second detector bank of the WISH instrument at ISIS pulsed neutron and muon source (UK). The green ticks indicate reflections allowed by the magnetic symmetry (space group $Pn'ma'$). The R_{wp} for this detector block is 3.70%.

TABLE I. Basis functions of the one-dimensional Γ-point irreducible representations found by decomposition of the magnetic representation for the iron site in NaFeF₃. The + and - symbols denote the relative sign of the magnetic moment along x, y, and z on the respective site.

Coordinate			Γ_1^+			Γ_2^+			Γ_3^+			Γ_4^+		
x	y	z	x	y	z	x	y	z	x	y	z	x	y	z
0.0	0.0	0.5	+	+	+	+	+	+	+	+	+	+	+	+
0.0	0.5	0.5	-	+	-	+	-	+	+	-	+	-	+	-
0.5	0.5	0.0	+	-	-	-	+	+	+	-	-	-	+	+
0.5	0.0	0.0	-	-	+	-	-	+	+	+	+	+	+	-

Γ-point representations (Table I) by Rietveld refinements against NPD at 2 K, and we found Γ_4^+ to precisely describe the magnetic ordering. This corresponds to the magnetic space group $Pn'ma'$ (Fig. 6).

The magnetic ordering of Γ_4^+ can be described as A$_x$ antiferromagnetic ordering along [001], F$_y$ ferromagnetic ordering along [010], and G$_z$ antiferromagnetic ordering along [001], corresponding to the refined parameters M_x, M_y, and M_z respectively (Table I). In our magnetic Rietveld refinements (Table II), we find a large value for the G$_z$ component (M_z) and a small value for the A$_x$ component (M_x). When performing Rietveld refinements of the ferromagnetic F$_y$ component, a value of $M_y = 0.75(3)\mu_B$ is obtained for the 2 K NPD data. However, since F$_y$ scattering coincides with nuclear peak positions, such quite small values of M_y yield very minor changes to the calculated diffraction pattern and agreement

factors. Furthermore, these are strong correlations with other parameters of the refinements, e.g., the thermal displacement parameter of Fe. The ZFC magnetization measurement furthermore suggests that the ferromagnetic moment should almost be absent at low temperatures without a magnetic field. As a consequence, the NPD data cannot be used to claim the existence of a F$_y$ component. Hence, M_y was fixed to zero during the final refinements.

Complete structural details obtained from the Rietveld refinements of NPD data is given in Table II, and in Supplemental Material [17] together with a visualization file. The refined model has a dominating G$_z$-type antiferromagnetic structure with moments aligned parallel to [001]. There are weak indications for a small canting parallel to [100] as given by the A$_x$ component (Fig. 6). The magnetic moments are antiferromagnetically oriented with respect to their nearest neighbors along [010], [101], and [$\bar{1}$01]. Neighboring spins are aligned close to the equatorial plane of the octahedra (defined by the four F2 atoms, Fig. 1) in the crystallographic (010) plane.

At 2 K the Rietveld refinements give a total ordered magnetic moment of 4.246(11) μ_B, slightly higher than the expected 4 μ_B for the four unpaired electrons of Fe²⁺. The value is in good agreement with that of Fe²⁺ in KFeF₃, which is 4.42 μ_B [23]. The slightly higher value than the expected total magnetic moment can be accounted for by an orbital contribution to the total magnetic moment measured by neutron diffraction. A very weak additional ferromagnetic component will not change this picture, but should not be neglected, see below.

The refinements (and magnetic peak intensities) show that the ordered magnetic moment decreases upon heating from 2 K. This is evidenced in the refined values for M_x and M_z [Fig. 7(a)]. The magnetic reflection in NPD disappears at 95 K, which is in compliance with the Néel temperature found by magnetometry.

We note the presence of a strong magnetostructural coupling in NaFeF₃, evidenced by major changes in the lattice parameters at the Néel ordering temperature [Figs. 7(b) and 7(c)]. At the transition, we observe a rather smooth contraction of the unit cell volume. However, this is an average of a contraction of the a-axis, in contrast to expansion of the b- and c-axis.

Already at 120 K, well above the ordering temperature, we observe a change in temperature dependence for the b axis (Fig. 7). Actually, by evaluating the difference intensity plot between NPD patterns at 95 and 120 K (close to and above the magnetic ordering temperature, respectively), we observe a
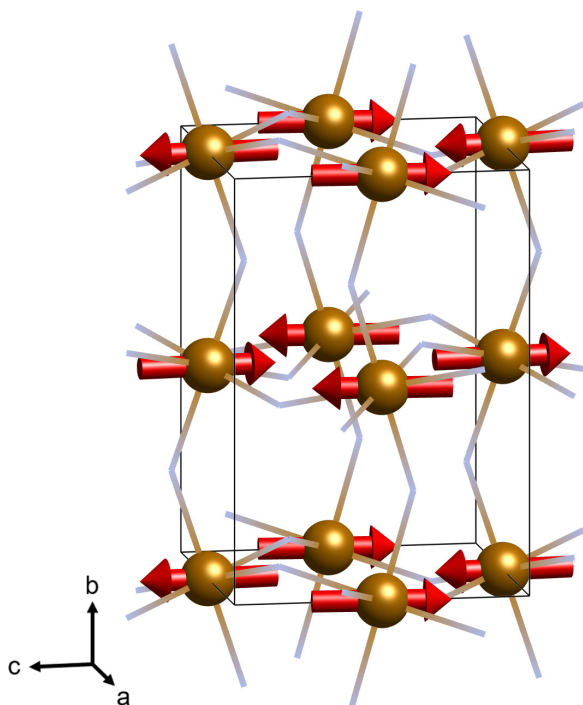

FIG. 6. Magnetic structure of the NaFeF₃ with magnetic space group $Pn'ma'$. The magnetic moments of the iron atoms are antiferromagnetically ordered relative to their nearest neighbors, yielding G-type antiferromagnetism. Iron atoms are shown in orange, and the bonds to fluorine as pale grey lines. Sodium atoms are removed for clarity.

TABLE II. Atomic coordinates of NaFeF$_3$ from Rietveld refinement of NPD at 2 K. The refinement was performed in magnetic space group $Pn'ma'$ with lattice parameters of $a = 5.62571(11)$ Å, $b = 7.87673(15)$ Å, and $c = 5.45623(10)$ Å, and magnetic parameters $M_x = 0.422(11)$ μ_B, $M_y = 0$ μ_B, and $M_z = 4.221(4)$ μ_B, yielding a total ordered magnetic moment of $M = 4.246(11)$ μ_B. The R_{wp} over all used detector blocks was 3.71%.

Site	Multiplicity	x	y	z	Occ	U_{iso} (Å^2)
Na	4	0.0544(2)	0.25	0.9826(3)	1	0.0175(4)
Fe	4	0.5	0	0	1	0.00438(17)
F1	4	0.45061(16)	0.25	0.11401(16)	1	0.0105(3)
F2	8	0.29707(11)	0.06114(8)	0.68918(11)	1	0.0096(2)

broad peak at around 4.8 Å (Fig. 8), which corresponds to the position of the (011)- and (110)-magnetic Bragg reflections in the ordered phase. The broad peak at 4.8 Å is thus interpreted as originating from the existence of short-range magnetic ordering just above the Néel temperature. Fe^{2+} is reported to display magnetostrictive behavior and diffuse scattering above T_N in Rb$_2$FeF$_4$, and we note that the diffuse scattering for NaFeF$_3$ above T_N also coincides with a tensile effect on the lattice [20].

As discussed above, due to a weak Jahn-Teller distortion, NaFeF$_3$ adopts short, medium, and long Fe-F bonds, see Fig. 1. Considering the variation of the Fe-F bond length between 2 and 297 K in the NPD experiment, we observe a clear trend: The bond lengths tend toward receiving identical values when temperature approaches 297 K (Fig. 9). In the cubic perovskite KFeF$_3$, the Fe-F bond lengths adopts a value

of 2.06 Å, which ought to be a value expected also for the Fe-F bond lengths in NaFeF$_3$ [21]. On this basis, it is tempting to suggest that NaFeF$_3$ may undergo transitions to higher symmetric structures at elevated temperatures [10,11]. This is beyond the scope of the present work.

IV. DISCUSSION

We highlight that our new wet-chemical synthesis protocol has allowed preparation of NaFeF$_3$ of very high purity, which is a prerequisite for clarification of inherent properties. Importantly, we compared ZFC–FC magnetic behavior of phase pure samples with reported data for samples made by a conventional solid-state method [10]. For NaFeF$_3$ prepared by our wet-chemical methods, the paramagnetic moment is within the expected range for Fe^{2+}. For NaFeF$_3$ prepared by solid-state methods, iron impurities easily outweigh the weak antiferromagnetic or paramagnetic signal, resulting in overestimated magnetization values. This is mirrored in the observation of ferromagnetic behavior in field scans at 300 K [10], which is not inherent to pure NaFeF$_3$.

χ'' in AC magnetometry indicates a ferromagnetic component appearing at 90 K, coinciding with the Néel temperature of NaFeF$_3$. Since a very weak additional reflection is observed by both diffraction techniques at low and high temperatures,
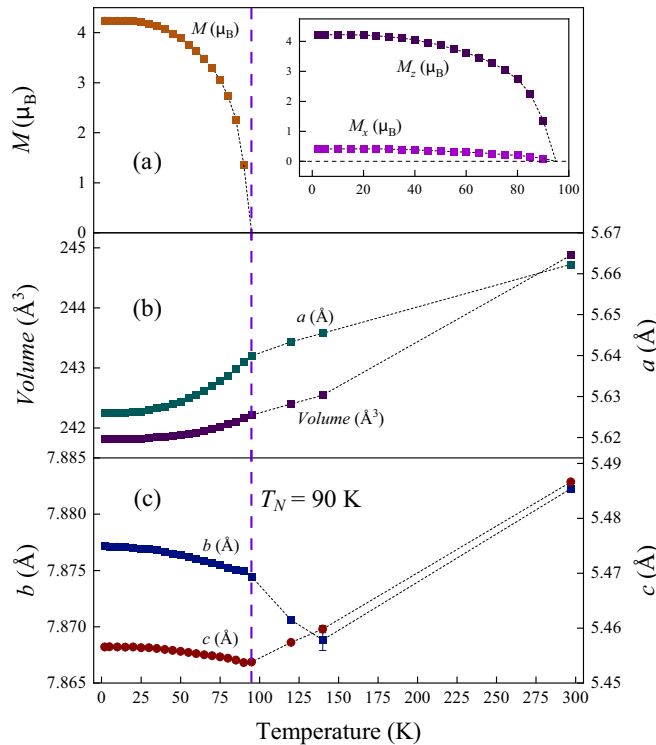

FIG. 7. Temperature dependence of structural parameters derived from Rietveld refinements of NPD; (a) the total magnetic moment, the inset shows the M_x and M_z components, (b) lattice parameter a and cell volume, and (c) lattice parameter b and c. The Néel temperature of 90 K is indicated by the purple dashed line.
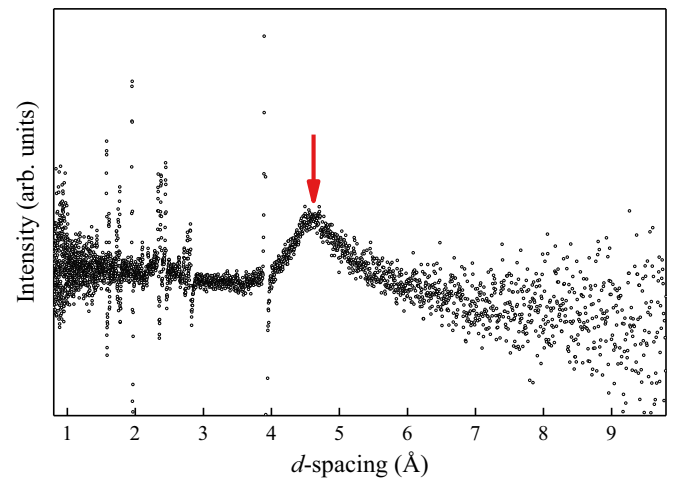

FIG. 8. Plot of the difference between NPD patterns at 95 and 120 K measured on the low-resolution detector bank. A broad peak around 4.8 Å is marked by a red arrow, which corresponds to the (011)- and (110)-magnetic Bragg reflections, and indicates short-range magnetic order appearing at 95 K.
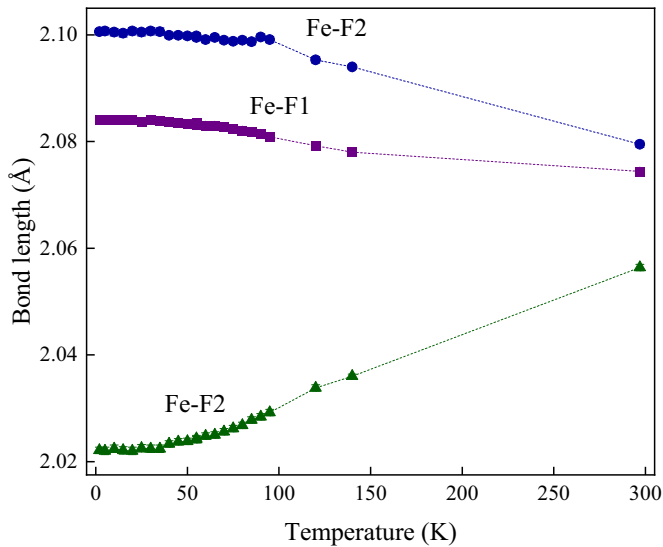
FIG. 9. Variation of the Fe-F bond lengths derived from Rietveld refinements of NPD between 2 and 297 K. Uncertainties are smaller than the symbol size.

one cannot fully rule out that the ferromagnetic component is due to an impurity phase. This peak does not correspond to any known ferromagnetic phase in the Na-Fe-F-O systems. Additionally, as the peak in χ'' appears at 90 K, we can exclude all ferromagnetic impurities with a high (> 90 K) Curie temperature. Hence, as the peak in χ'' appears at the Néel temperature of $NaFeF_3$, we interpret this as is a strong signature of an inherent weak ferromagnetic component for $NaFeF_3$, but as indicated by the DC magnetometry and field scans, one with a ferromagnetic moment close to zero.

Although a ferromagnetic component is indicated by a distinct peak in the imaginary component χ'' of the AC susceptibility, NPD cannot unambiguously conclude on the possible existence of a symmetry allowed ferromagnetic component along [010] (F_y) according to the magnetic space group $Pn'ma'$. Considering the magnetic F-Fe-F interactions of $NaFeF_3$ in light of the Goodenough-Kanamori-Anderson (GKA) rules, antiferromagnetism is expected [22]. Furthermore, a linear G-type magnetic structure was predicted by DFT for $NaFeF_3$ [10], also with moments arranged along [001] (G_z-type). However, our Rietveld analysis considered an additional weak A_x component, which implies canting of the antiferromagnetism. The latter component is close to the detection limit of the analysis.

G-type magnetic ordering is observed in several other fluoroperovskites, e.g., KMF_3 ($M = $ Mn, Fe, Co, and Ni) [23].

However, due to the small sodium cation and the weakly Jahn-Teller active Fe^{2+}, the structure of $NaFeF_3$ is significantly distorted and the F-Fe-F bond angles deviate from $180°$. As a consequence, the interactions may deviate from the GKA rules.

Correspondingly, one must consider other magnetic interactions as origin to the weak ferromagnetism. For compounds with d^6 electron configuration Jahn-Teller, as well as spin-orbit interaction mechanism, will contribute to stabilization of the system [24]. If spin-orbit coupling is present in $NaFeF_3$, Dzyaloshinskii-Moriya interactions may occur, which is in compliance with the orbital contribution to the total magnetic moment found by neutron diffraction. Such interactions give rise to ferromagnetic exchange, and may thus be the origin of weak ferromagnetism in $NaFeF_3$ [25,26].

V. CONCLUSION

In summary we have developed a wet-chemical synthesis protocol that allow preparation of $NaFeF_3$ in large quantities and of high purity. As a consequence we have been able to investigate the inherent magnetic properties of $NaFeF_3$ without potential additional magnetic contributions from impurities like α-Fe and Fe_3O_4 that will interfere with the analysis. Magnetic susceptibility and powder neutron diffraction analysis show that $NaFeF_3$ has a Néel temperature of 90 K. AC magnetometry indicate the presence of weak ferromagnetism inherent to $NaFeF_3$ below the ordering temperature, supported by field dependent DC measurements. Neutron diffraction data describe the compound as a weakly canted G_z-type antiferromagnet, with a minor A_x-component allowed by symmetry. The magnetic space group opens for a F_y component, however this is almost absent at zero field and is too weak to be proven by the current analysis. The temperature variation of the Fe-F bonds suggests a possible structural phase transition to a higher symmetric structure above 300 K.

[1] M. Leblanc, V. Maisonneuve, and A. Tressaud, Chem. Rev. **115**, 1191 (2015).

[2] A. Tressaud, J. Fluorine Chem. **132**, 651 (2011).

[3] R. M. Dubrovin, L. N. Alyabyeva, N. V. Siverin, B. P. Gorshunov, N. N. Novikova, K. N. Boldyrev, and R. V. Pisarev, Phys. Rev. B **101**, 180403(R) (2020).

[4] R. M. Dubrovin, S. A. Kizhaev, P. P. Syrnikov, J.-Y. Gesland, and R. V. Pisarev, Phys. Rev. B **98**, 060403(R) (2018).

[5] H. Béa, M. Gajek, M. Bibes, and A. Barthélémy, J. Phys. Condens. Mat. **20**, 434221 (2008).

[6] I. Žutić, J. Fabian and S. Das Sarma, Rev. Mod. Phys. **76**, 323 (2004).

[7] A. Kitajou, H. Komatsu, K. Chihara, I. D. Gocheva, S. Okada, and J. Yamaki, J. Power Sources **198**, 389 (2012).

[8] Y. Yamada, T. Doi, I. Tanaka, S. Okada, and J. Yamaki, J. Power Sources **196**, 4837 (2011).

[9] K. V. Kravchyk, T. Zünd, M. Worle, M. V. Kovalenko, and M. I. Bodnarchuk, Chem. Mater **30**, 1825 (2018).

[10] F. L. M. Bernal, K. V. Yusenko, J. Sottmann, C. Drathen, J. Guignard, O. M. Løvvik, W. A. Chrichton, and S. Margadonna, Inorg. Chem. **53**, 12205 (2014).

[11] W. A. Chrichton, F. L. M. Bernal, J. Guignard, M. Hanfland, and S. Margadonna, Mineral. Mag. **80**, 659 (2016).

[12] J. M. De Teresa, M. R. Ibarra, P. Algarabel, L. Morellon, B. Garcia-Landa, C. Marquina, C. Ritter, A. Maignan, C. Martin, B. Raveau, A. Kurbakov, and V. Trounov, Phys. Rev. B **65**, 100403(R) (2002).

[13] A. Coelho, J. Appl. Cryst. **51**, 210 (2018).

[14] L. C. Chapon and P. Manuel, Neutron News **22**, 22 (2011).

[15] O. Arnold, J. C. Bilheux, J. M. Borreguero, A. Buts, S. I. Campbell, L. Chapon, M. Doucet, N. Draper, R. Ferraz Leal, M. A. Gigg, V. E. Lynch, A. Markvardsen, D. J. Mikkelson, R. L. Mikkelson, R. Miller, K. Palmen, P. Parker, G. Passos, T. G. Perring, P. F. Peterson, S. Ren, M. A. Reuter, A. T. Savici, J. W. Taylor, R. J. Taylor, R. Tolchenov, W. Zhou, and J. Zikovsky, Nucl. Instrum. Methods Phys. Res. A **764**, 156 (2014).

[16] V. Petříček, M. Dušeka, and L. Palatinus, Z. Kristallogr. **229**, 345 (2014).

[17] See Supplemental Material at http://link.aps.org/supplemental/10.1103/PhysRevMaterials.4.114412 for VESTA file visualization of magnetic structure, tables on structural and magnetic details, and XRD and NPD patterns at 2 and 297 K.

[18] F. L. M. Bernal, J. Sottmann, D. S. Wragg, H. Fjellvåg, Ø. S. Fjellvåg, C. Drathen, W. A. Sławiński, and O. M. Løvvik, Phys. Rev. Materials **4**, 054412 (2020).

[19] A. Szytuła, M. Bałanda, B. Penc and M. Hofmann, J. Phys.: Condens. Matter **12**, 7455 (2000).

[20] R. J. Birgeneau, H. J. Guggenheim, and G. Shirane, Phys. Rev. B **1**, 2211 (1970).

[21] R. J. Birgeneau, H. J. Guggenheim, and G. Shirane, Acta Cryst. B **39**, 561 (1983).

[22] J. B. Goodenough, *Magnetism and the Chemical Bond* (R. E. Krieger Publishing Company, 1976).

[23] V. Scatturin, L. Corliss, N. Elliott, and J. Hastings, Acta Cryst. **14**, 19 (1961).

[24] K. I. Kugel' and D. I. Khomskiǐ, Sov. Phys. Usp. **25**, 231 (1982).

[25] I. Dzyaloshinsky, J. Phys. Chem. Solids **4**, 241 (1958).

[26] T. Moriya, Phys. Rev. **120**, 91 (1960).